Isothermal shear-induced heat flow

András Baranyai,* Denis J. Evans, and Peter J. Daivis
Research School of Chemistry, Australian National University, G.P.O. Box 4, Canberra, Australian Capital Territory, 2601, Australia
(Received 2 March 1992; revised manuscript received 27 July 1992)

By performing molecular-dynamics simulations of a fluid under the influence of a sinusoidal transverse force, we point out that heat flow can be induced in the absence of a temperature gradient. This heat flux is observed to be proportional to the gradient of the square of the strain-rate tensor. We show that this shear-gradient-induced heat flux is of the same order in the pressure gradient as the heat flow produced by viscous heating.

PACS number(s): 03.40.Gc, 02.50.+s, 51.10.+y, 05.70.Ln

I. INTRODUCTION

In this paper we perform nonequilibrium-molecular-dynamics simulations of a fluid subject to a sinusoidal transverse force. This force, directed in the x direction, is a function of the y coordinate, and thus induces a sinusoidal transverse velocity gradient. If the wavelength of the transverse force field is sufficiently large, one can use the observed values of the transverse velocity field or the sinusoidal shear stress to calculate the shear viscosity of the fluid. Indeed, the "sinusoidal transverse force" method (STF) [1] was one of the earliest methods proposed for calculating the shear viscosity of fluids. This method is not competitive with modern homogeneous shear methods such as the Sllod algorithm [2] (so named because of its close relationship to the Dolls tensor algorithm).

Our purpose in studying the STF system is not to obtain estimates of the shear viscosity but rather is to study the complex interactions between heat and mass flows that arise in inhomogeneous shear flows. Because the strain rate varies sinusoidally with respect to position, the STF induces a sinusoidal temperature gradient with a spatial frequency which is double that of the velocity profile. The amplitude of the temperature modulation is at small fields, proportional to the square of the applied field. These temperature modulations drive a sinusoidal heat flux whose magnitude is again proportional to the square of the applied STF.

One could, of course, also study these interactions by modeling boundary-driven Poiseuille or Couette flows using molecular dynamics [3]. We do not do this because: (a) atomic packing effects at the boundaries manifest in strong density oscillations, propagate long distances [3] into the bulk of the fluid, and (b) such simulations are vastly more expensive in computer time, requiring tens or even hundreds of thousands of particles rather than the 1000 particles used in the present work [3].

Using Gauss's principle of least constraint [2], a number of variations were possible. In addition to thermostatting the zero-wave-vector component of the temperature field, we designed equations of motion which allowed us to independently control the amplitudes of the harmonic modulations of the temperature field and the heat flux vector.

When simulations were carried out in a system where the temperature modulations were suppressed, we observed something quite surprising. We observed that in the absence of harmonic temperature modulations, a heat flux was still observed to flow from regions of high strain rate to those of lower shear. Further, the magnitude of this isothermal, shear-induced heat flux was observed to be proportional to the square of the applied STF and hence does not vanish when compared to the temperature-driven heat flux, in the linear zero STF limit.

In the following sections we describe the methods used to carry out these simulations; then we review the results before discussing some of the implications of the isothermal shear-induced heat flux for both hydrodynamics and for irreversible thermodynamics.

II. DESCRIPTION OF THE STF SYSTEM

A. Characterization of a fluid under a STF

The sinusoidal transverse force method of Gosling *et al.* [1,4] is less convenient and much less efficient than the homogeneous Sllod algorithm [2] for calculating the shear viscosity of dense fluids. The sinusoidal external field $F_x(y)$, defined as

$$F_x(y)=F_{x1}\sin(q_1 y)\ , \tag{1}$$

where $q_1=(2\pi/L_y)$, and L_y is the length of the molecular dynamics cell in the y direction, generates a y-dependent streaming x-velocity profile. The amplitude of the modulation is determined by the magnitude of the constant, F_{x1}. Because the shear rate $\gamma\equiv\partial u_x/\partial y$ is dependent on the y coordinate, the whole system can be viewed as a collection of *open* nonequilibrium steady-state (ness) systems characterized by different shear rates, in mutual thermal and mechanical contact. The neighboring fluid layers can exchange heat and mass, and can establish mechanical equilibrium. These properties make the sinusoidal transverse force system an interesting model for studying the conditions of thermal "equilibrium" between Ness systems.

For sufficiently small F_{x1} we expect the induced velocity field to take the form

$$u_x(y)=\sum_n u_x(q_n)\sin(q_n y)\ , \quad n=1,3,5\ldots\ , \tag{2}$$

where $q_n=(2\pi n/L_y)$. In the linear regime where $F_{x1}\to 0^+$, $u_x(q_1)$ is the only nonzero term. At higher fields the odd harmonics only are excited. This is because the velocity profile must be symmetric about $y=L_y/4$ and $3L_y/4$. For very high fields and high Reynolds numbers the induced velocity field becomes turbulent. In this work we only consider the weak nonlinear regime, where only the odd harmonics are excited.

Starting from the Fourier expansion of the velocity profile (2), we can describe the variations of all the important properties of the system. The velocity profile implies a strain rate profile, $du_x/dy=\gamma(y)$:

$$\gamma(y)=\sum_n q_n u_x(q_n)\cos(q_n y)\ , \quad n=1,3,5,\ldots\ . \tag{3}$$

The xy element of the pressure tensor, P_{xy}, also exclusively involves odd cosine harmonics,

$$P_{xy}(y)=\sum_n P_{xy}(q_n)\cos(q_n y)\ , \quad n=1,3,5,\ldots\ . \tag{4}$$

Since the variations in the temperature, the number and energy density and the diagonal elements of the pressure tensor are proportional to γ^2, their expansions can only involve even cosine harmonics. For example the y dependence of the temperature profile must be expressible as

$$T(y)=\sum_n T(2q_n)\cos(2q_n y)\ , \quad n=1,2,3,\ldots\ . \tag{5}$$

The y component of the heat flux vector J_{Qy} is proportional to dT/dy, and thus should involve only even sine harmonics:

$$J_{Qy}(y)=\sum_n J_{Qy}(2q_n)\sin(2q_n y)\ , \quad n=1,2,3,\ldots\ . \tag{6}$$

The correctness of these expansions was tested during the course of the simulations, confirming that the omitted terms are really zero within statistical uncertainties.

The determination of the coefficients of the expansions can be done directly, utilizing the instantaneous microscopic representations of the relevant quantities in Fourier space [2]. An alternative way to do this is the least-squares fit of the expansion [2]. We used the latter method to determine the streaming velocity $u_x(y)$. In this method, $u_x(y)$ is defined as that velocity which minimizes the sum of squares of deviations from the particle velocities, $p_{ix/m}$. Let R be that sum of squares

$$R=\sum_{i=1}^{N}\left[\frac{p_{ix}}{m}-\sum_n u_x(q_n)\sin(q_n y_i)\right]^2\ . \tag{7}$$

Equating the derivatives of (7) with respect to $u_x(q_m)$, to zero we find

$$\frac{\partial R}{\partial u_x(q_m)}=2\sum_{i=1}^{N}\left[\frac{p_{ix}}{m}-\sum_n u_x(q_n)\sin(q_n y_i)\right]\sin(q_m y_i)=0\ . \tag{8}$$

The above matrix equation is solved at every time step during the simulation to obtain the coefficients of the Fourier expansion for $u_x(y)$. It has been shown [2] that the least-squares method described by (7) and (8) gives a correct expression for the Fourier space decomposition of the velocity field.

All of the other properties can be determined either by the least-squares-fitting procedure or by direct expansion. The averages of the properties for the entire system were taken as the zero-wave-vector terms of the expansion. It is important to note, however, that unlike the case of homogeneous shear, the calculated system properties are highly interrelated. For instance, the estimate for the streaming velocity determines the peculiar velocities of the particles, $\mathbf{c}_i\equiv\mathbf{p}_i/m-\mathbf{u}(\mathbf{r}_i)$. This is then used to compute the y-dependent peculiar kinetic-energy density $K(y)$ of the peculiar kinetic energy $K=\sum_i mc_i^2/2$. Having determined the y dependence of the number density $n(y)$, the y dependence of the kinetic temperature can be determined from the equation

$$T(y)=\frac{2K(y)}{gk_B n(y)}\ , \tag{9}$$

where g is the dimensionality of space. The kinetic temperature $T(y)$ is then used in a feedback mechanism to thermostat the system. This means that the determination of the Fourier coefficients must follow a hierarchical order.

B. The thermostatting mechanism

Since the continuous work done by the external field (1) is transformed into heat, we need a mechanism which removes this heat in order to maintain a NESS. Thermostatting techniques for homogeneous systems are well known and well understood. We will need to distinguish two features of these deterministic thermostats. First, we need to know the algebraic *form* of the thermostatting equations. This form involves a thermostatting multiplier, usually written as α. In all routinely used thermostats, the form of the equations is obtained from Gauss's principle of least constraint [2]. Having determined the form of thermostatting equations, an expression for the thermostatting multiplier α needs to be obtained. At this stage a variety of approaches are possible. Such an expression can be determined from the Gauss principle (in this case α becomes a phase function), or α can be treated as an extra coordinate in the system satisfying an integral feedback equation, as in the Nosé-Hoover method [2,5]. The critical element of constructing a thermostat is the determination of the *form* of the thermostatting equations.

To fix the zero-wave-vector component of the temperature profile, Gauss's principle shows that the form of the thermostatting equations of motion is

$$\begin{aligned}\dot{\mathbf{r}}_i&=\frac{\mathbf{p}_i}{m}\ ,\\ \dot{\mathbf{p}}_i&=\mathbf{F}_i+\mathbf{i}F_x(y_i)-\alpha_0[\mathbf{p}_i-m\mathbf{i}u_x(y_i)]\ .\end{aligned} \tag{10}$$

The thermostatting multiplier α_0 can then be treated either as a differential or integral feedback multiplier and

evaluated from either Gauss's principle or a Nosé-Hoover equation.

In order to determine the form of equations of motion that are required to fix the nonzero-wave-vector components of the temperature profile, we again appeal to Gauss's principle. From Eq. (9) we see that

$$\dot{T}(y)=\frac{2\dot{K}(y)}{gk_B n(y)}-\frac{\dot{n}(y)T(y)}{n(y)}\ . \tag{11}$$

If we Fourier transform this equation, we see that the time derivative of the wave-vector-dependent temperature profile is

$$\begin{aligned}\dot{T}(q)&=\int dy\left[\frac{2\dot{K}(y)}{gk_B n(y)}-\frac{\dot{n}(y)T(y)}{n(y)}\right]e^{iqy}\ ,\quad q=2q_n \text{ for } n=1,2,3,\ldots\\&=\int dy\left[\frac{2\sum_i \dot{K}_i\delta(y_i-y)}{gk_B n(y)}-\frac{\dot{n}(y)T(y)}{n(y)}\right]e^{iqy}\\&=\sum_i\frac{m[\mathbf{p}_i/m-\mathbf{i}u_x(y_i)][\dot{\mathbf{p}}_i/m-\mathbf{i}\dot{u}_x(y_i)]e^{iqy}}{gk_B n(y_i)}-\int dy\left[\frac{\dot{n}(y)T(y)}{n(y)}\right]e^{iqy}\ .\end{aligned} \tag{12}$$

From Gauss's principle we know that the form of the thermostatting equations of motion required to ensure that $dT(q)/dt=0$ is determined by the *coefficient* of acceleration in the differential form of the constraint equation [2]. This can be read quite simply from Eq. (12), since the last term on the right-hand side does not involve particle accelerations. The form of the thermostatting equations of motion is therefore

$$\begin{aligned}\dot{\mathbf{p}}_i=&\mathbf{F}_i+\mathbf{i}F_x(y_i)\\&-\left[\alpha_0+\sum_n\frac{\alpha_n}{n(y_i)}\cos(2q_n y_i)\right][\mathbf{p}_i-m\mathbf{i}u_x(y_i)]\ ,\\&\qquad n=1,2,3,\ldots,\end{aligned} \tag{13}$$

where $\mathbf{r}_i$, $\mathbf{p}_i$, and $\mathbf{F}_i$ are the position, momentum, and interatomic force on particle i. $\mathbf{i}$ is the unit vector in the x direction, α_0 is the usual thermostatting multiplier which fixes the temperature of the *whole* system (i.e., the average temperature), while the α_n terms fix the Fourier components of the temperature profile. Expressed in words rather than mathematics, we see that in order to fix the various Fourier components of the temperature, we remove random kinetic-energy *density* (i.e., peculiar kinetic energy per particle) at the corresponding wave vector and phase.

Using Nosé-Hoover feedback, the equations for the various thermostatting multipliers α_n can be written as

$$\dot{\alpha}_0=\frac{T-T_0}{Q_0}\ ,\quad \dot{\alpha}_n=\frac{T_n(2q_n)-T_{n0}(2q_n)}{Q_n}\ , \tag{14}$$

where T is the instantaneous, zero-wave-vector kinetic temperature of the whole system, T_0 is the target value, and Q_0 is an undetermined intensive constant which controls the time scale of the Nosé-Hoover feedback. Analogously, the second equation of (14) constrains the coefficients of the Fourier expansion of the temperature.

Before passing to the technical details of the calculations, some remarks are in order concerning the thermodynamic state of the system. Our NESS has three independent state variables. These three variables are the average temperature T, the average number density n, and the amplitude of the external sinusoidal field F_{x1}. Because the external field is inhomogeneous, it generates inhomogeneities in the temperature profile and the local number density. With the use of our thermostat we can control the low-wave-vector amplitudes of the temperature profile.

Because the NESS is by definition in mechanical equilibrium, the yy element of the pressure tensor, $P_{yy}(y)$, is constant. One can apply a second external field to eliminate the low-wave-vector density variations, but this will then destroy the constancy of P_{yy}. Under the sinusoidal external field F_{x1}, one cannot simultaneously eliminate the temperature, density, and P_{yy} variations.

III. DETAILS OF THE CALCULATIONS

The calculations were performed for systems of both 540 and 1080 WCA particles [6]. The WCA potential as a function of distance r is $\phi(r)=4(r^{-12}-r^{-6})+1$ if $r<2^{1/6}$ and zero otherwise. All simulations were performed at a zero-wave-vector kinetic temperature T_0 of 0.722 and at an overall density of 0.8442.

The simulation box length in the y direction L_y should be chosen long enough to ensure that for the two or three lowest nonzero wave vectors, $q=4\pi/L_y$, $6\pi/L_y$, the transport coefficients, in particular the thermal conductivity λ, and the shear viscosity η, are equal to their zero-wave-vector values, within statistical uncertainties. This can be done economically by replacing the usual cubic shape of the simulation box with a rectangular box which contains several cube-shaped cells in the y direction. We used two systems: the smaller one with $N=540$ particles employed a unit cell of 5×108 particle cubes ($L_y=25.194$), while the larger system employed 10×108 particle cubes ($L_y=50.388$).

We used three types of simulations. The overall temperature of the system was fixed in all three cases ($T_0=0.722$). Type-I simulations employed only a zero-wave-vector temperature constraint ($\langle T\rangle=T_0=0.722$, $\alpha_{n\neq 0}=0$). In type-II calculations we also constrained the

first harmonic $[\cos(2q_1y)]$ of the temperature profile to be zero ($\langle T\rangle = T_0 = 0.722$, $\langle T_1(2q_1)\rangle = 0$, $\alpha_{n>1} = 0$), while in type-III simulations we adjusted the value of $T_i(2q_1)$ to that value required to set the first term in the heat flux vector expansion to zero ($\langle T\rangle = T_0 = 0.722$, $\langle J_{Qy}(2q_1)\rangle = 0$, $\alpha_{n>1} = 0$). This is easily done by replacing the second equation in (14) with the following feedback equation for the first-harmonic temperature multiplier:

$$\dot{\alpha}_1 = \frac{J_{Qy}(2q_1)}{Q_1} . \tag{15}$$

We calculated only the first four symmetry-allowed terms in each harmonic expansion. The convergence was very rapid, with the third- and fourth-order terms often being barely distinguishable from zero. In principle all of the coefficients of the temperature expansion could be fixed. In practice, however, it is difficult to constrain the higher-order terms due to their small values and high spatial frequency. Thus the constraints in type-II and -III simulations have been made only in the first term of either the temperature and heat flux expansions. This fact does not seriously limit our calculations for two reasons. First, the higher-order terms, in most of the cases, are essentially noise, being orders of magnitude smaller than the leading nonzero harmonic. Secondly, there are no direct couplings between higher-order terms and those of lower order. For example, the first term of the heat flux vector $[\sin(2q_1y)]$ can only be generated by the gradient of the first term of the temperature $[\cos(2q_1y)]$ but not by higher-order terms.

We performed a sequence of simulations for both system sizes ($N = 540$ or 1080) and calculated the coefficients of the Fourier expansion as a function of the amplitude F_{x1} of the sinusoidal external field for several properties. The largest possible amplitude of the external field was determined by the numerical stability of the program. For the larger system the maximum useful value of F_{x1} was four times smaller than for the smaller system.

The length of the calculations was 200 000 time steps ($\Delta t = 0.004$). Unlike equilibrium or homogeneous nonequilibrium simulations, the time necessary to reach a steady state is reasonably long for the STF system. This is caused by the interrelated nature of the expansion, as we alluded to above. We performed at least 50 000 time steps of equilibration before collecting averages. In Table I we summarize the simulations that were carried out. Unless otherwise stated, the calculations refer only to the first symmetry-allowed coefficient of the respective expansions, and we refer to the kinetic temperature defined by (9) as simply the temperature.

IV. RESULTS

In Fig. 1 we show u_{x1} as a function of F_{x1} for all three types of simulations performed on the smaller system ($N = 540$). The large modulations in the streaming velocity for type I are substantially reduced if the temperature profile (type II) or even more if the heat current (type III) is fixed to zero. The convergence of the velocity expansion is good, particularly for smaller external fields and for simulations of type II and III. The difference between the first and second terms of the expansion is at worst one and at best three orders of magnitude. In Table II we show the first three coefficients of the velocity expansion for 540 particles (type I). The first term in the strain rate expansion is $\gamma_1 = q_1 u_{x1}$, where $q_1 = 0.2494$ for $N = 540$ or 0.1247 for $n = 1080$. We can obtain a direct estimate for the viscosity η_{d1} from the constitutive relation $P_{xy1} = -\eta_{d1}\gamma_1$. Alternatively, the viscosity can be calculated from the amplitude of the first harmonic of the velocity field induced by the applied STF,

$$\eta_{h1} = \frac{nF_{x1}}{q_1^2 u_x(q_1)} . \tag{16}$$

This equation is easily derived by substituting Eq. (1) into the Navier-Stokes equation [4]. The viscosity values calculated either way can be used as a crosscheck of the simulations. In Tables II and III we see excellent agreement between η_{d1} and η_{h1} in the linear limit, where the linear Navier-Stokes equation can be expected to be valid.

In Fig. 2 we show η_{d1} as a function of $\gamma_1^{1/2}$. The straight line is a fit [7] of the homogeneous planar Couette simulations of $N = 2048$ WCA particles using the Sllod algorithm [2]. The largest discrepancies from the homogeneous simulations can be seen in the type-I calculations when the temperature and the density changes from layer to layer and there is also a heat flow in the y direction. The η_{d1} values of the other two types of simulation are close to the corresponding Sllod values. In the small-field limit all three types of calculations correctly approach the zero strain rate limiting value. The results shown in Fig. 2 show that the shear viscosity is affected by the presence of induced heat flows. The figure clearly

TABLE I. List of simulations performed (x = 200 000 time steps) for types I, II, and III for $N = 540$ and 1080.

$N = 540$				$N = 1080$			
I	II	III	$F_{x1}(540)$	I	II	III	$F_{x1}(1080)$
x	x	x	0.05	x	x	x	0.05
x	x	x	0.10	x	x	x	0.10
x	x	x	0.20	x	x	x	0.15
x	x	x	0.40	x	x	x	0.20
x	x	x	0.60		x	x	0.25
x	x	x	0.80				

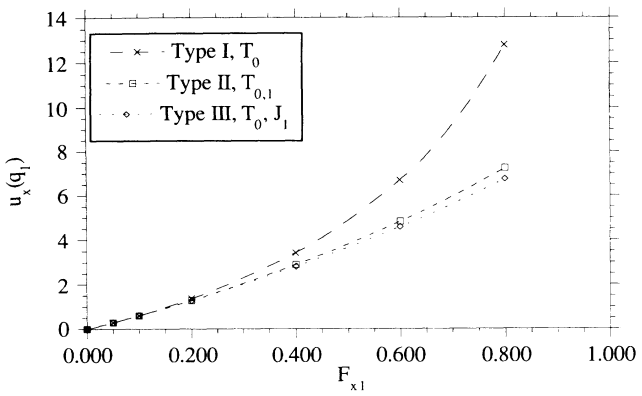

FIG. 1. The first allowed harmonic of the velocity that is induced by the STF. In type-I simulations, denoted T_0, the zero-wave-vector temperature is fixed but the higher harmonics of the temperature and heat flux are free. In type-II simulations, denoted $T_{0,1}$, the zeroth and first harmonics of the temperature are fixed (the first harmonic is set to zero), while in type-III simulations, denoted T_0,J_1, the zeroth-temperature harmonic and the first allowed heat flux harmonic are fixed (again the heat flux harmonic is set to zero). $N=540$.

shows that the results from the sinusoidal transverse force algorithm agree most closely with the homogeneous Sllod algorithm when the induced heat flux is removed (type III). Estimates of the homogeneous flow shear viscosity obtained using the type-I STF method are quite inaccurate at larger strain rates.

In Fig. 3 we show J_{Qy1} as a function of F_{x1}. In the unconstrained case (type I), energy is transferred from the high to the low shear regions of the liquid. The heat current increases substantially with the field as it might be expected.

For type-II simulations where the first symmetry-allowed harmonic in the temperature field is set to zero, heat continues to flow from the high to the low shear regions. Heat flow is generated in the absence of a temperature gradient. The heat flux J_{Qy1} increases with γ_1 or equivalently with F_{x1}.

The simplest phenomenological explanation for this surprising behavior is to postulate a new constitutive relation which predicts that a heat flux will be generated not only by temperature gradients but also by a gradient in the square of the strain rate:

$$\mathbf{J}_Q=-\lambda\nabla T-\xi\nabla(\nabla\mathbf{u}:(\nabla\mathbf{u})^T)\ . \tag{17}$$

(Note there are no contributions to the y heat flux arising from $\nabla^2\mathbf{u}$, since this term is parallel to the x axis.) In type-II simulations the coupling coefficient ξ, which describes the isothermal generation of heat flux by a gradient in the square of the strain rate, can be evaluated directly, since the first allowed harmonic of ∇T is zero. In type-III simulations the ratio ξ/λ can be easily calculated, since $\mathbf{J}_Q$ is zero.

In Fig. 4 we see that for the unconstrained case (type I) the temperature of the high shear regions is much higher than that of the low shear regions. The amplitude of the modulation increases with the external field until it reaches saturation, where the amplitude approaches the absolute value of the kinetic temperature. At such strong fields the temperature of low shear regions is close to zero, i.e., these layers are solid. Type-II results are not shown in the figure because T_1 is zero for this case. Since in type-III simulations the heat flux is zero, T_1 must be negative in order to cancel the heat flux generated from $\nabla\gamma^2$. This means that at zero heat flux (type III), the kinetic temperature of a high shear region is lower than the kinetic temperature of a coexisting low shear region.

In Fig. 5 we show the first term of the number density expansion ρ_1. The maximum variation in ρ_1 is 0.8442. Since ρ_1 is not constrained, it varies with the external field for all three types of calculations. For type I it also approaches saturation at the highest fields, while for type III the changes are quite small. All the changes in the density are negative, which is simply a manifestation of shear dilatancy. The high shear layers have lower density than the low shear layers.

In Fig. 6 we show the heat flux (J_{Qy1}) as a function of $d\gamma_1^2/dy$ for simulations of type II. The curves for both systems have very similar characteristics, although for the larger system we had to confine the simulations to much smaller variations in γ. This similarity shows that for $N>\sim 540$ the number dependence of our results is slight. From our postulated constitutive relation (17), we see that the derivative of J_{Qy1} (type II) with respect to $d\gamma_1^2/dy$ gives the cross coupling coefficient ξ, which gets smaller for stronger fields. The derivative does not seem to either diverge to infinity or decrease to zero in the zero-field limit. This suggests that the form of (17) is correct and that ξ should not, for instance, be defined in terms of $d|\gamma_1|/dy$. In Fig. 7 we show ξ as a function of $d\gamma_1^2/dy$.

Another interesting property of this system is that the heat flux (J_{Qy1}) for type-II simulations is proportional to $-P_{xy}\gamma$, which is proportional to the work done by the external field on each liquid layer (see Fig. 8). This leads to the important conclusion that in the small-field limit

TABLE II. The first three symmetry-allowed terms of the velocity expansion (2) for $N=540$ as a function of F_{x1} for type-I simulations. We also show values of η_{h1} and η_{d1}.

F_{x1}	$n=1$	$n=3$	$n=5$	η_{h1}	η_{d1}
0.05	0.302	−0.002	0.002	2.25	2.24
0.10	0.612	0.002	−0.001	2.22	2.22
0.20	1.377	0.033	0.001	1.97	1.98
0.40	3.435	0.206	−0.006	1.58	1.64
0.60	6.709	0.480	−0.026	1.21	1.30
0.80	12.792	−0.006	−0.269	0.85	0.93

TABLE III. We show values of η_{h1} and η_{d1} for $N=1080$ simulations of the three types.

F_{x1}	I	II	III
		η_{d1}	
0.05	2.102	2.222	2.246
0.10	1.784	2.098	2.118
0.15	1.364	1.978	2.009
0.20	1.203	1.885	1.913
		η_{h1}	
0.05	2.089	2.226	2.252
0.10	1.724	2.097	2.118
0.15	1.242	1.973	2.011
0.20	1.074	1.876	1.911

$F_{x1}=0^+$, the heat flux induced by the temperature gradient is of the same order in the field as the heat flux induced by the gradient in the strain rate.

Having determined ξ values as a function of $d\gamma_1^2/dy$ from the type-II simulations, we can calculate the thermal conductivity using Eq. (17) from type-I and type-III simulations. These calculations of the thermal conductivity can then be compared with a completely independent calculation of the same quantity using the standard NEMD algorithm for thermal conductivity [2]. In Fig. 9 we compare the thermal conductivities for the $N=540$ system. In the figure, λ(I) and λ(III) denote the thermal conductivities obtained from type-I and -III simulations. The thermal conductivity obtained from the standard algorithm is denoted simply by λ. The x axis denotes the applied heat field in the standard NEMD algorithm, J_{Qy1}/λ in the type-I simulations and $2q_1T_1/T$ for type-III simulations. With this choice for the x axis we can perform an approximate comparison of the nonlinear dependence of the thermal conductivities obtained by the various methods. It is only in the zero-heat-field, linear regime that the standard NEMD algorithm is known to predict the correct thermal conductivity [2]. As can be clearly seen from the figure, all three estimates of the thermal conductivity are in excellent numerical agreement with each other.

In Fig. 9 we also show the thermal conductivity that would be obtained from type-I simulations if one ignored the effects of our postulated shear induced heat flux (i.e., if one simply determined the thermal conductivity by dividing the heat flux by the temperature gradient). It can be clearly seen that these results, denoted $\lambda+\xi\nabla\gamma^2/\nabla T$, overestimate the true thermal conductivity by about 25%. This overestimate is much larger than the statistical uncertainties of any of the estimates for the thermal

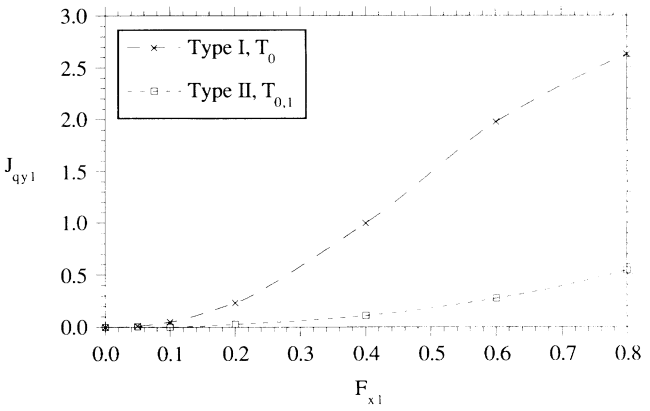

FIG. 3. The first allowed heat flux harmonic as a function of the STF for $N=540$. For type-III simulations this harmonic is constrained to zero. Surprisingly, although the temperature is uniform in type-II simulations, heat continues to flow from the high shear to the low shear regions. This means that estimates of the thermal conductivity from type-I simulations will overestimate the thermal conductivity because previously they did not take account of the isothermal shear-induced heat flow shown here.

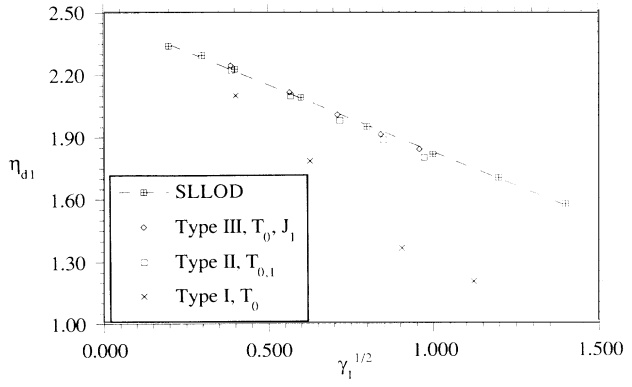

FIG. 2. Estimates of the shear viscosity obtained from $N=1080$ STF simulation with the conventional homogeneous Sllod algorithm ($N=2048$). Clearly, the nonlinear viscosity of type-I simulations is different from the homogeneous nonlinear viscosity. The nonlinear viscosities obtained at constant temperature, type II, and zero heat flux, type III, agree very well with the homogeneous viscosity. In the zero shear rate linear limit all techniques are in agreement.

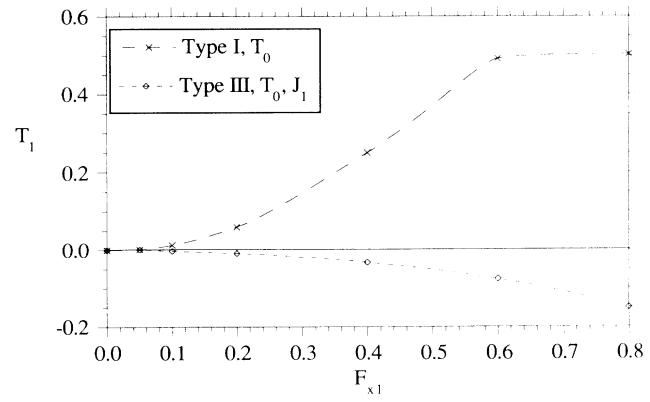

FIG. 4. The first allowed temperature harmonic as a function of the applied field for $N=540$. For type-II simulations this harmonic is zero. In order to maintain a zero heat flux (type III), the temperature must be reduced in the high shear region in order to cancel the heat flux that occurs in the absence of a temperature gradient.

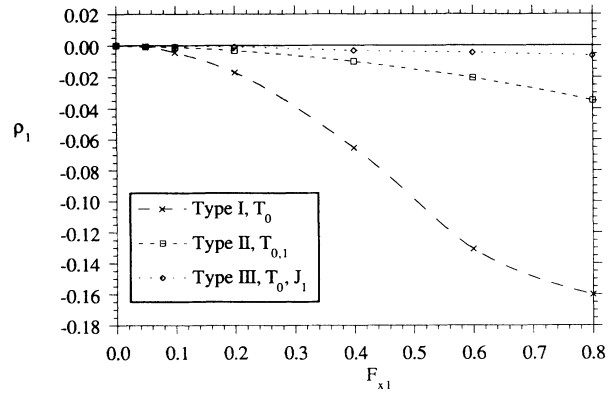

FIG. 5. The first allowed density harmonic as a function of the STF for $N=540$.

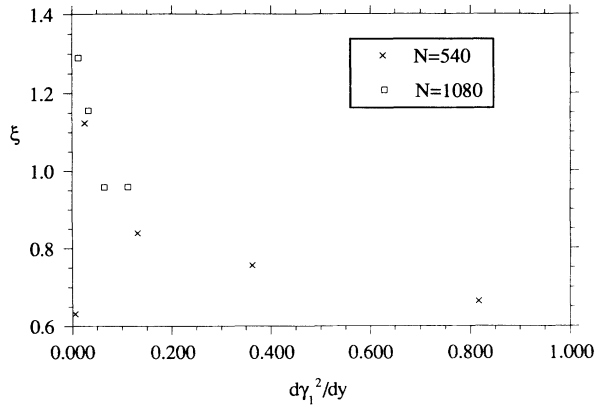

FIG. 7. The cross coupling coefficient ξ as a function of $\nabla(\gamma_1^2)$.

conductivity, and results from the fact that in type-I simulations the heat flux is the *sum* of the heat flux induced by the temperature gradient and the heat flux induced by the gradient in the strain rate.

V. CONCLUSIONS

Our calculations show that a uniform temperature in nonequilibrium systems does *not* guarantee that the heat flux will be zero. We have interpreted our numerical experiments by introducing a cross-coupling term which couples a gradient in the square of the shear rate to the heat flux. The fact that by using this postulate we can correctly predict the thermal conductivity from sinusoidal transverse force simulations, while in the absence of the postulate one would overestimate the thermal conductivity by 25% strongly supports the correctness of our postulate. Our postulated constitutive relation means that in systems where the shear rate is not uniform in space, as in planar Poiseuille flow, then no matter how close the system is to equilibrium, the heat flux generated by the variations in the strain rate is of the same order as that generated from the shear-induced temperature differences.

We will now apply our proposed constitutive relation (17) to a simple hydrodynamic problem, namely planar Poiseuille flow. Consider a fluid sandwiched between two parallel plates separated by a distance b. We assume the plates are located at the planes $y=0$ and b. We use stick boundary conditions and assume that the two plates are maintained at a fixed temperature T_p. The flow is generated by a constant pressure head, $H=\partial p/\partial x$.

Since the heating and the shear-induced heat flux effects are second order in the pressure head while the induced velocity profile is of linear order in H, we will ignore the possible effects of heating upon the velocity profile. The solution for the velocity profile $u_x(y)$ is therefore

$$u_x(y)=\frac{-H}{2\eta}y(b-y)+O(H^2)\ . \tag{18}$$

For this geometry, the leading-order heat equation is

$$\rho c_v\frac{dT}{dt}=\lambda\nabla^2T+\xi\nabla^2\left[\frac{\partial u_x}{\partial y}\right]^2+\eta\left[\frac{\partial u_x}{\partial y}\right]^2, \tag{19}$$

where we have used our constitutive relation (17) for both

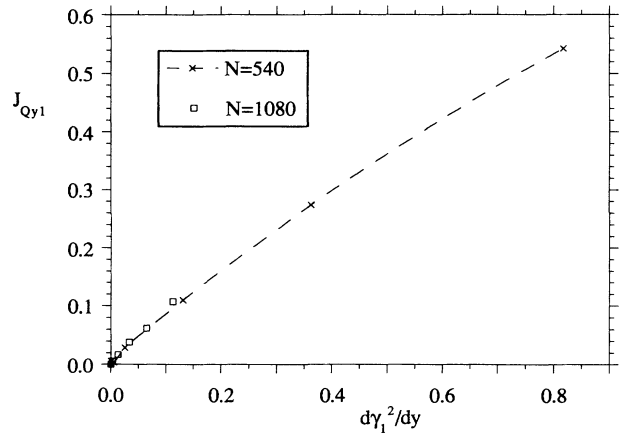

FIG. 6. The first allowed harmonic of the heat flux as a function of $\nabla(\gamma_1^2)$ for both system sizes. These curves are only weakly dependent on system size. These results were obtained from type-II simulations. The ratio of the heat flux to $\nabla(\gamma_1^2)$ gives the cross-coupling coefficient ξ.

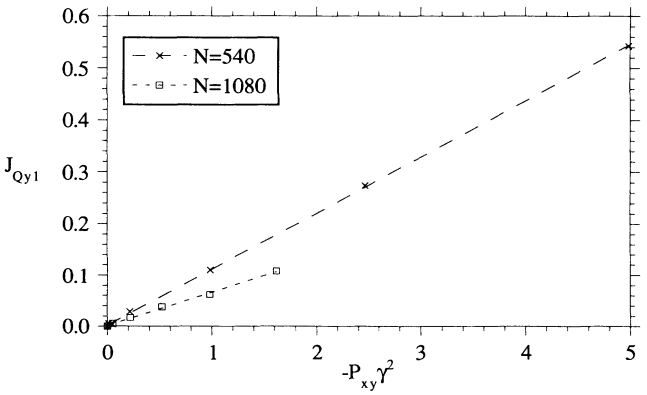

FIG. 8. The heat flux is for type-II simulations, a linear function of the viscous heating rate.

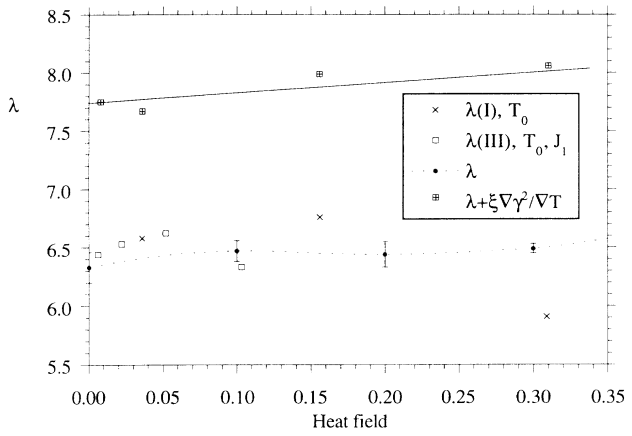

FIG. 9. The thermal conductivity computed from type-I [λ(I)] and type-III [λ(III)] simulations agrees with that obtained independently using the standard NEMD algorithm (λ) for thermal conductivity. If one ignores the effects of isothermal shear induced heat flow ($\lambda+\xi\nabla\gamma^2/\nabla T$), one overestimates the thermal conductivity by ~25%.

thermally induced and shear-induced heat flux together with the knowledge that the divergence of the velocity profile is zero.

The equation for the steady-state temperature profile is

$$\frac{d^2T(y)}{dy^2}=-\frac{\xi}{\lambda}\frac{d^2\gamma^2(y)}{dy^2}-\frac{\eta}{\lambda}\gamma^2(y)\ , \tag{20}$$

where $\gamma(y)$ is the strain rate $\partial u_x/\partial y$. We can solve this equation using the solution (18) to the velocity equation. We find that the leading-order steady-state temperature profile is

$$T(y)=-\frac{\xi(\partial p/\partial x)^2}{4\eta^2\lambda}(b-2y)^2 -\frac{(\partial p/\partial x)^2}{192\eta\lambda}(b-2y)^4+D\ , \tag{21}$$

where the integration constant D is related to the wall temperature $T_p=T(0)=T(b)$ and is equal to $\xi(\partial p/\partial y)^2b^2/4\eta^2\lambda+(\partial p/\partial y)^4b^4/192\eta\lambda+T_p$. This equation shows that in the zero-flow limit, the contribution to the temperature profile arising from the shear induction term is of the same order as the usual temperature-driven term and is of order $(\partial p/\partial x)^2$. The shear-induction term will dominate when $(b-2y)<\sqrt{48\xi/\eta}$. The shear-induction term will change the shape of the temperature profile near the center of the flow, from quartic to parabolic, and could have important consequences for highly inhomogeneous flows in narrow channels, i.e., in lubricating contacts. For *planar* Couette flow, the contribution to the temperature profile from the shear-induction term is identically zero because (apart from the Knudsen layer) the strain rate is constant and therefore $\nabla\gamma^2=0$.

A recent simulation of boundary-driven Couette flow by Liem, Brown, and Clarke [3] offers some support for the presence of quadratic terms in the temperature profile for Poiseuille flow. They performed a molecular-dynamics simulation of the flow of some 40 000 atoms between moving boundaries that were modeled atomically. Because of velocity slip at the boundaries, the velocity profile was observed to be a nonlinear function of the position within the channel. In their calculations they certainly did observe "significant deviations" from the simple hydrodynamic prediction of a parabolic temperature profile. Unfortunately, their paper contains insufficient information to make a quantitative comparison with our work.

Our present work points out a difficulty with attempts to propose a nonequilibrium generalization of the zeroth law of thermodynamics. It would be natural to postulate that when two steady-state systems have the same "thermodynamic" temperature when under steady-state conditions, heat ceases to flow from one system to the other. If we apply this postulated zeroth law to our sinusoidal transverse force system, we arrive at a paradox. Considering fluid layers at different y coordinates as coexisting steady-state systems, our results predict that close to equilibrium, layers with identical kinetic temperatures have strain-rate-dependent "thermodynamic temperatures," and that those layers with the higher strain rate have the higher "thermodynamic" temperature. The difference between these two "temperatures" would be proportional to γ^2. Recent computer experiments using the Green expansion [8] for the entropy S suggest that based on the definition $T=(\partial E/\partial S)|_{V,\gamma}$, the thermodynamic temperature decreases with increasing strain rate at constant energy and volume [9].

ACKNOWLEDGMENT

We would like to thank the Australian National University Supercomputer Facility for a generous grant of computer time.

*Permanent address: Laboratory of Theoretical Chemistry, Eötvös University, Budapest Múzeum krt 6-8, 1088 Hungary.

[1] E. M. Gosling, I. R. McDonald, and K. Singer, Mol. Phys. **26**, 1475 (1973).

[2] D. J. Evans and G. P. Morriss, *Statistical Mechanics of Nonequilibrium Liquids* (Academic, New York, 1990).

[3] S. Y. Liem, D. Brown, and J. H. R. Clarke, Phys. Rev. A **45**, 3706 (1992).

[4] D. J. Evans, Mol. Phys. **47**, 1165 (1982).

[5] S. Nosé, J. Chem. Phys. **81**, 511 (1984); Mol. Phys. **52**, 255 (1984); W. G. Hoover, Phys. Rev. A **31**, 1695 (1985).

[6] J. D. Weeks, D. Chandler, and H. C. Andersen, J. Chem. Phys. **54**, 5237 (1971).

[7] D. J. Evans, G. P. Morriss, and L. M. Hood, Mol. Phys. **68**, 637 (1989).

[8] H. S. Green, *The Molecular Theory of Fluids* (North-Holland, Amsterdam, 1952); A. Baranyai and D. J. Evans, Mol. Phys. **74**, 353 (1991).

[9] D. J. Evans, J. Stat. Phys. **74**, 745 (1989).